The influence of nickel substitution on the structural and gas sensing properties of sprayed ZnFe$_2$O$_4$ thin films

S. B. Madake[1,2] , A. R. Patil[1], R. S. Pedanekar[1], N. A. Narewadikar[1], J. B. Thorat[2], and K. Y. Rajpure[1,*]

[1] *Electrochemical Materials Laboratory, Department of Physics, Shivaji University, Kolhapur, MS 416004, India*
[2] *Department of Physics, Sadguru Gadage Maharaj College, Vidyanagar, Karad, MS 415124, India*

ABSTRACT

A comparative study of spray-deposited Ni$_x$Zn$_{1-x}$Fe$_2$O$_4$ (x = 0 to 0.5) thin films has been performed specifically on their structural and gas sensing properties. The films were characterized by X-ray diffraction and field emission scanning electron microscopy. The structural and morphological study reveal the formation of nanocrystalline cubic spinel structure with porous surface morphology. The Rietveld refinement study shows the crystalline structure and it gives proper atomic distribution among spinel sites. The gas sensing study indicates the selectivity of material toward SO$_2$ gas. The study of dependence between the optimal operating temperature and nickel substitution shows a reduction in the operating temperature of the sensor. The optimized film with composition Ni$_{0.3}$Zn$_{0.7}$Fe$_2$O$_4$ shows the maximum response to SO$_2$ gas at a lower operating temperature of 130 °C. These results can be applied in designing low energy consumption SO$_2$ gas sensors.

1 Introduction

The utility of ferrites varies according to their structural and morphological properties. All these properties depend on their method of synthesis and preparative parameters. Many researchers prepared metal-substituted zinc ferrite and studied their physiochemical properties. Some particular compositions of mixed ferrite are found efficient in specific applications [1–7]. The utility of ferrites varies according to their composition and structural and morphological properties. The physicochemical properties depend upon the method of synthesis and preparative parameters. Many researchers studied the physicochemical properties of metal-substituted zinc ferrite. Some particular compositions of such mixed ferrite were found efficient in specific applications [1, 2]. The ferrites with the general chemical formula MFe$_2$O$_4$ (M = divalent metal) exhibit the cubic spinel structure. It consists of two atomic sites for divalent metal ions and trivalent Fe ions, namely, tetrahedral (A) site and octahedral (B) site. The

distribution of metals among these sites decides the spinel type, either normal or inversed. If the divalent metal ions wholly occupy A-site, then it is called normal spinel, and if they occupy B-site, it is said to be inverse spinel, while the condition of spinel in which metals are partially distributed in both sites is known as random or mixed spinel. Many reports underlined the effect of site occupancies on the properties of ferrites. The multicomponent ferrite shows variety in occupancies, which make them versatile in technological applications [8].

Many researchers reported the Ni–Zn ferrite as a potential gas sensing candidate for various gases in gas sensing applications. Kapse et al. [9] studied gas sensing properties of $Ni_{0.6}Zn_{0.4}Fe_2O_4$. They prepared the powder by ethylene glycol-mediated citrate sol–gel method. The material shows selective sensitivity toward ethanol at 300 °C. Kazin et al. [10] prepared fine nanocrystalline powders of $Ni_xZn_{1-x}Fe_2O_4$ by spray pyrolysis and studied their NH_3 gas sensing properties by virtue of their cation distribution. Ebrahimi et al. [11] synthesized $Ni_{0.5}Zn_{0.5}Fe_2O_4$ using the co-precipitation method and checked their gas sensing properties toward acetonitrile. Dalawai et al. [12] prepared $Ni_xZn_{1-x}Fe_2O_4$ by oxalate co-precipitation method and checked their LPG, Cl_2, and ethanol sensing properties.

In the present work, the study is focused on the synthesis of nickel-substituted zinc ferrite thin films $Ni_xZn_{1-x}Fe_2O_4$ ($x = 0$ to 0.5) for gas sensing application. The structural properties of the films were analyzed by Rietveld refinement of their X-ray diffraction (XRD) patterns. In gas sensing study, the effect of nickel content on optimal operating temperature and gas response of prepared thin films has been studied.

2 Experimental

2.1 Materials

Zinc nitrate hexahydrate ($Zn(NO_3)_2 \cdot 6H_2O$) (98.5%), ferric nitrate nonahydrate ($Fe(NO_3)_3 \cdot 9H_2O$) (99%), and nickel nitrate trihydrate ($Ni(NO_3)_2 \cdot 3H_2O$) (99%) were purchased from Thomas Baker Chemicals, Mumbai (India) and ammonium chloride (NH_4Cl) (99%) and conducting silver paste were obtained from Alfa Aesar, Mumbai (India). The test gases were purchased from Spacecryo Pvt. Ltd., Mumbai. All the chemicals were used without further purification. Double-distilled water was used to make solutions throughout the synthesis process.

2.2 Deposition of $Ni_xZn_{1-x}Fe_2O_4$ thin films

Nickel-substituted zinc ferrite thin films $Ni_xZn_{1-x}Fe_2O_4$ ($x = 0$ to 0.5) were deposited on the glass substrates using the spray pyrolysis technique. Firstly, the aqueous solutions of 0.1 M nickel nitrate, zinc nitrate, and iron nitrate were prepared separately. These solutions were mixed in volumetric ratio x:1–x:2, respectively, further 1% w/v ammonium chloride was added in it as porogen [13]. 10 ml of this mixed solution was sprayed intermittently over clean glass substrates preheated at 375 °C. After each successive spray of 10 s, a halt of 30 s was taken. The carrier gas (compressed air) flowed uniformly at a constant pressure 0.5 bar, the solution flow rate was adjusted to 2.5 ml/min, and the distance between the spraying nozzle and substrates was 30 cm. The deposited brown-colored uniform thin films were allowed to cool naturally to room temperature. All these films were air annealed at 500 °C for 5 h in a muffle furnace. The films were named as per their Ni content; the films with fraction $x = 0$, 0.1, 0.2, 0.3, 0.4, and 0.5 as N0, N1, N2, N3, N4, and N5, respectively.

2.3 Characterization

The deposited films were characterized by XRD, field emission scanning electron microscopy (FESEM), energy-dispersive X-ray spectroscopy (EDX), and spectroscopic ellipsometry for their structural, morphological, elemental, and thickness study, respectively. The XRD patterns were recorded on Bruker, D2 Phaser diffractometer in the 2θ range from 10° to 90° using CuKα radiation having wavelength 1.5418 Å. The XRD patterns were refined using *FullProf* software to get crystallographic information. The surface morphology was captured on Tescan Mira3 field emission scanning electron microscope. The elemental composition was studied using Oxford Instrumentations EDX attached to FESEM. The thicknesses of the films were calculated on J. A. Woollam, alpha-SE ellipsometer, by simulating the data using the B-Spline model in CompleteEase software. Chemiresistive measurements were recorded using the computer-interfaced Keithley electrometer, 6514/E.

2.4 Preparation of sensing element and gas sensing measurements

The sensing elements were prepared by painting two silver electrodes on prepared films using conducting silver paste. The sensing elements were placed in the chamber of a lab-made two probe gas sensing unit having an inbuilt heating assembly. The contact probes were connected to an electrometer, where the real-time resistance of the sensor was recorded. After confirming proper contact between the silver electrode and probes, the sensor element was allowed to heat at the desired temperature. When the temperature reached the desired value, the test gas was injected into the chamber. Time-dependant resistance values were used to calculate the gas response using the formula, $[\Delta R/R_0] \times 100\%$, where ΔR is a change in resistance of sensor element upon exposure of test gas and R_0 is its resistance in the air.

3 Results and discussion

3.1 Structural, morphological, and elemental studies

The Rietveld-refined XRD patterns of nickel-substituted zinc ferrite thin films are shown in Fig. 1. These films are polycrystalline and exhibit cubic spinel structure. The indexed peaks (111), (220), (311), (400), (422), (511), and (440) of zinc ferrite and nickel-substituted zinc ferrite samples match with JCPDS Card Nos. 01-089-4926 and 00-008-0234, respectively. The positions of diffraction peaks are shifted slightly toward larger diffraction angles on substitution of Ni^{2+}. The shift arises due to the mismatching of ionic radii of Ni^{2+} and Zn^{2+}. The ionic radius of Ni^{2+} is lesser than Zn^{2+}. As a result, the substitution of Ni^{2+} in $ZnFe_2O_4$ reduces the lattice constant of the crystal. A similar result was reported by Kumbhar et al. [14, 15], Surendran et al. [16], Gao et al. [17], and Guo et al. [18]. The average crystallite sizes of all samples were calculated using Scherrer's formula and are found to be 16 ± 3 nm.

Table 1 gives the Rietveld refinement factors, such as chi-square (χ^2), weighed profile factor (R_{wp}), expected weighed profile factor (R_{exp}), Bragg factor (R_B) and crystallographic factor (R_F), cell parameter (a), cell volume (V), and density (ρ) of $Ni_xZn_{1-x}Fe_2O_4$ thin films. The agreement factor χ^2 is defined as the

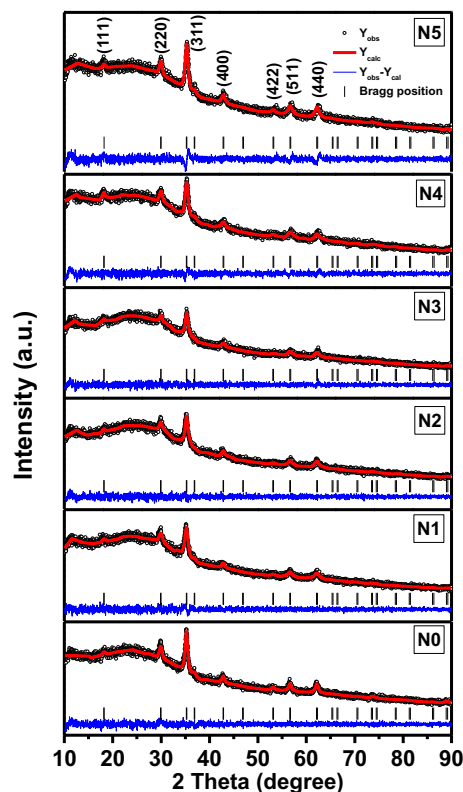**Fig. 1** Rietveld-refined XRD patterns of $Ni_xZn_{1-x}Fe_2O_4$ ($x = 0$ to 0.5) thin films

square of the ratio of weighed and expected R factors as $\chi^2 = (R_{wp}/R_{exp})^2$. In this study, this factor was found to be varied from 1.05 to 1.31. The refinement confirms a reduction in lattice constant (a) and hence the shrinking of lattice upon substituting Ni^{2+} ions. The increased density of substituted films is also a consequence of reduced lattice size. Substitution of Ni^{2+} ions in $ZnFe_2O_4$ host lattice affected cation distribution from both lattice sites. All the Ni^{2+} ions and a maximum number of Zn^{2+} ions from tetrahedral A-site occupy octahedral B-site in the N1 sample. In other cases, only a small amount of Ni^{2+} and Zn^{2+} occupies A-site. The occupancy of Ni-A and Zn-A increased from 0 to 0.03 and 0 to 0.05, respectively, in nickel-substituted films. The result tells that the Zn ions combined with Ni ions have a maximum tendency to occupy B-site in spinel lattice.

The position coordinates and refined occupancies of elements in $Ni_xZn_{1-x}Fe_2O_4$ are summarized in Table 2. The cation distribution calculated from Rietveld refinement is given in Table 3. The atomic arrangements in N3 are shown in Fig. 2.

Table 1 Rietveld refinement factors of $Ni_xZn_{1-x}Fe_2O_4$ thin films

Rietveld refinement factors	N0	N1	N2	N3	N4	N5
χ^2	1.06	1.09	1.05	1.08	1.17	1.31
R_B	6.49	5.41	6.80	4.54	3.96	6.07
R_F	7.39	5.61	7.95	3.98	3.70	5.82
R_{wp}	50.5	56.6	65.8	64.8	49.3	53.2
R_{exp}	49.08	54.26	64.25	62.21	45.65	46.48
a (Å)	8.4475	8.4462	8.4447	8.4434	8.4422	8.4413
V (Å^3)	602.82	602.54	602.22	601.94	601.68	601.49
ρ (g/cm^3)	5.313	5.409	5.452	5.554	5.66	5.707

The surface morphologies of prepared films are depicted in Fig. 3. The film N0 and N1 show grains of different sizes and shapes with intergranular pores. Film N2 also shows the same morphology, but the grains are indistinctive. Film N3 shows a rough morphology of distinct grains, while films N4 and N5 show interconnected morphology, like lichen. The roughness and porous nature of films afford a high surface-to-volume ratio which helps to enhance the interactions between gas molecules and surface [20, 21]. The ellipsometric simulations gave the thickness of all films around 500 nm. Figure 4 shows the EDX spectrum of the N3 sample; it indicated the presence of O, Fe, Ni, and Zn as principal elements. The EDX result confirms the composition of the prepared sample with ratios close to the theoretical values (Table 4).

3.2 Gas sensing properties

The gas response of the metal oxide semiconductors depends on the operating temperature and the composition of the sensing material. The gas response of prepared thin films of various compositions $Ni_xZn_{1-x}Fe_2O_4$ ($x = 0$ to 0.5) toward SO_2 gas was studied as a function of operating temperature.

Figure 5 shows the responses of prepared films with respect to operating temperature. Each film

Table 3 Cation distribution in $Ni_xZn_{1-x}Fe_2O_4$ thin films

Sample	Cation distribution
N0	$(Fe_{0.74}Zn_{0.26}Ni_{0.0})_A[Fe_{1.26}Zn_{0.74}Ni_{0.0}]_BO_4$
N1	$(Fe_{0.97}Zn_{0.03}Ni_{0.0})_A[Fe_{1.03}Zn_{0.87}Ni_{0.10}]_BO_4$
N2	$(Fe_{0.97}Zn_{0.02}Ni_{0.01})_A[Fe_{1.03}Zn_{0.78}Ni_{0.19}]_BO_4$
N3	$(Fe_{0.99}Zn_{0.00}Ni_{0.01})_A[Fe_{1.01}Zn_{0.70}Ni_{0.29}]_BO_4$
N4	$(Fe_{0.93}Zn_{0.05}Ni_{0.02})_A[Fe_{1.07}Zn_{0.55}Ni_{0.38}]_BO_4$
N5	$(Fe_{0.92}Zn_{0.05}Ni_{0.03})_A[Fe_{1.08}Zn_{0.45}Ni_{0.47}]_BO_4$
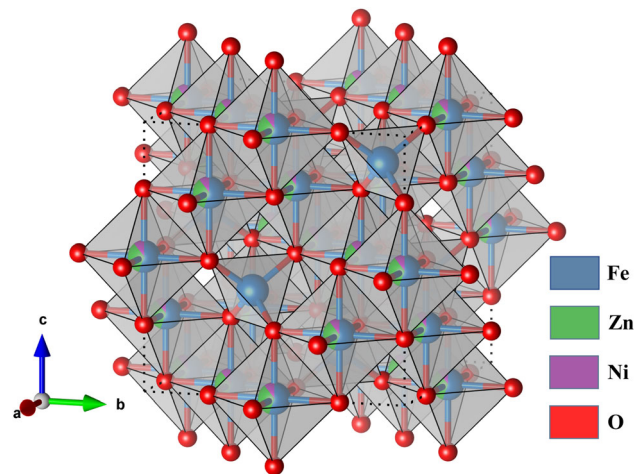
Fig. 2 Atomic arrangements of N3 drawn in VESTA software [19] using Rietveld-refined parameters

Table 2 Atomic coordinates and occupancies from Rietveld refinement of XRD of $Ni_xZn_{1-x}Fe_2O_4$ thin films

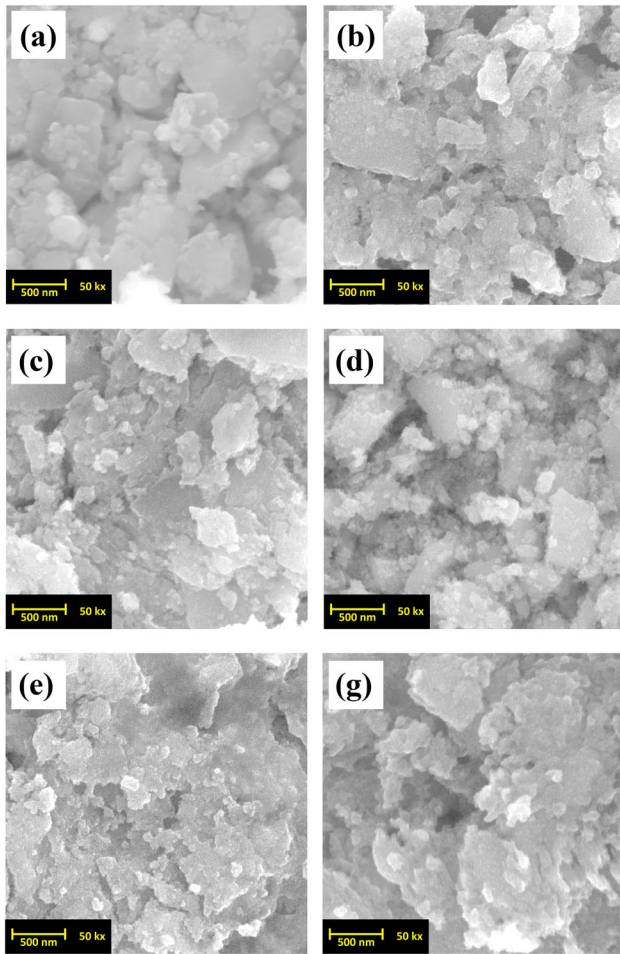| Atoms	Lattice sites	Atomic coordinate	Occupancy					
		$x = y = z$	N0	N1	N2	N3	N4	N5
Fe	A	0.125	0.74	0.97	0.97	0.99	0.93	0.92
Fe	B	0.5	0.63	0.515	0.515	0.505	0.535	0.54
Zn	A	0.125	0.26	0.03	0.02	0.00	0.05	0.05
Zn	B	0.5	0.37	0.435	0.39	0.35	0.275	0.225
Ni	A	0.125	0.00	0.00	0.01	0.01	0.02	0.03
Ni	B	0.5	0	0.05	0.095	0.145	0.19	0.235

Fig. 3 FESEM image of $Ni_xZn_{1-x}Fe_2O_4$ thin film

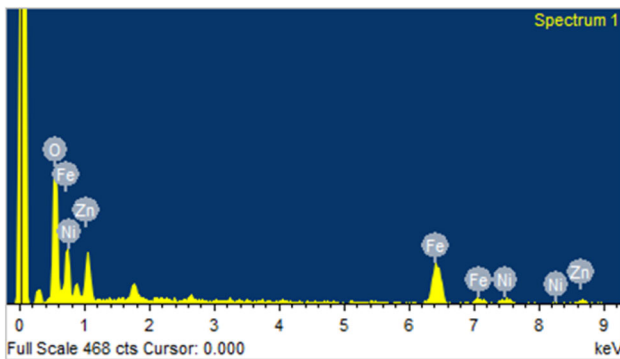**Fig. 4** EDX spectrum of $Ni_{0.3}Zn_{0.7}Fe_2O_4$ (N3) thin film

Table 4 Elemental ratio from EDX

Elemental ratio	Observed	Expected
Ni/Zn	0.415	0.429
(Ni + Zn)/Fe	0.548	0.5

showed increasing response up to a particular temperature above which it declined. The temperature at which the films showed the highest response is taken to be their optimal operating temperature. The reaction between analyte gas molecules and surface-adsorbed oxygen species at lower temperatures is too slow to give a high response. But as the operating temperature increases, the analyte gas molecules activate enough to overcome the activation energy barrier to react with more oxygen species. Further, at higher temperatures, some gas molecules escape from the sensor surface before reaction due to their enhanced activation, so at higher temperatures, the adsorption and diffusion of gas are limited; therefore, the response decreases [22–24]. The temperature at which the film showed maximum response was considered as its optimal operating temperature.

The films N0, N1, N2, N3, N4, and N5 show their optimal operating temperature to be 150 °C, 140 °C, 130 °C, 130 °C, 140 °C, and 140 °C, respectively. It proves that the substitution of the Ni^{2+} ions by replacing Zn^{2+} improves the sensing behavior. Among all the thin films, N3 shows the highest response at minimum operating temperature. It shows a 64% response at 130 °C operating temperature. This enhanced gas sensing activity is a consequence of appropriate Ni^{2+} substitution, catalytic activity, and the porous morphology of film [25].

According to the accepted mechanism, the oxygen molecules from surrounding air are adsorbed on the film surface and up to 150 °C they transform into $O_{2(ads)}^-$ ionic species by capturing electrons from the
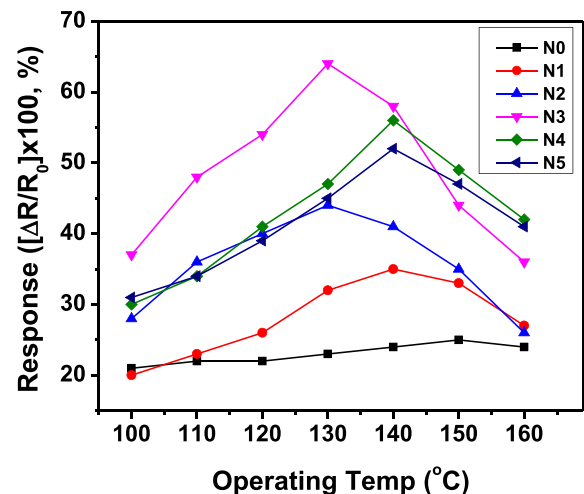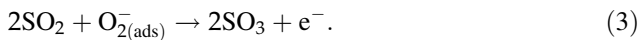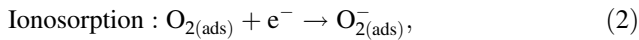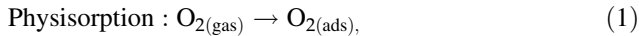

Fig. 5 Variation of responses of thin film for 100 ppm SO_2 gas with respect to operating temperature

bulk of the material. The SO_2 gas molecules react with these active oxygen species on the sensor surface and convert them into SO_3 by donating electrons to the conduction band of the sensing material. The mechanism is given below [26, 27]:

$$\text{Physisorption}: O_{2(gas)} \rightarrow O_{2(ads),} \tag{1}$$

$$\text{Ionosorption}: O_{2(ads)} + e^- \rightarrow O_{2(ads)}^-, \tag{2}$$

$$2SO_2 + O_{2(ads)}^- \rightarrow 2SO_3 + e^-. \tag{3}$$

The conversion of SO_2 to SO_3 requires a higher temperature, but in the presence of a catalyst, the efficient conversion occurs at lower temperatures [28]. In fact, without the catalyst, the oxidation of SO_2 is very hard, even at higher temperatures [29]. In the SO_2 gas sensing process, the sensor material acts as a catalyst for the conversion of SO_2 to SO_3.

The reported operating temperatures of ferrite-based SO_2 gas sensors are given in Table 5. Various forms of sensor design, like thin film, thick film, pellet, of these materials, have been reported. Yang et al. [30] reported the 650 °C operating temperature for $NiFe_2O_4$ thick-film gas sensor. Van Hoang et al. [31] and Hsiao et al. [32] reported SO_2 response at temperatures above 300 °C in the case of reduced graphene oxide (RGO)-loaded $ZnFe_2O_4$ and Fe_3O_4, respectively. Palimar et al. [33] and Queraltó et al. [34] reported the lanthanum ferrite-based bulk materials as efficient SO_2 sensors working below 300 °C. Aranthady et al. [35] reported SO_2 sensing properties of $La_{0.6}Ca_{0.4}FeO_3$ in pellet and thin-film form. They found different optimal operating temperatures in both cases; the pellet form of the sensor showed the highest response at 160 °C, while the thin-film form showed 120 °C. With this brief survey, one can conclude that the thin-film architecture of the mixed material composition of metal oxides can show the enhanced gas response at lower temperatures.

The response–recovery curve of the N3 sample upon exposure of 100 ppm SO_2 gas at 130 °C is shown in Fig. 6. It attained 90% of the maximum response value in 30 s. On venting the target gas, the response reduced steadily and reached 10% of the initial response in 150 s. Variation of N0 and N3 film response upon exposure of 5 to 600 ppm SO_2 gas at 150 °C and 130 °C, respectively, are shown in Fig. 7. The response of N0 film found increased linearly up to 200 ppm, but in the case of N3, the linear response is found only up to 100 ppm gas exposure; further,

the response found saturated. N3 showed a 2.8% response for 5 ppm and 64% response for 100 ppm exposure. Furthermore, the increment in response slowed down and reached only up to 88%, even at 600 ppm of SO_2 exposure.

Figure 8 shows the selectivity plot comparing the responses of acetone, ethanol, LPG, and SO_2 gases at 100 ppm exposure concentration. The selectivity measurements were performed at 100 ppm exposure of these gases at 130 °C operating temperature. The film response toward the LPG, ethanol, and acetone is around 20–25%, but it showed good selectivity toward SO_2 with almost three times higher response than the other gases. The order of response is SO_2 >> acetone > ethanol > LPG. Cyclic exposures of 100 ppm SO_2 gas to the better responding film N3 at its optimal operating temperature 130 °C showed nearly 9% decrement in response after 100 repeated exposures, as shown in Fig. 9.

4 Conclusion

Porous nanocrystalline $Ni_xZn_{1-x}Fe_2O_4$ thin films having approximately 500 nm thickness were deposited using the spray pyrolysis technique. The average crystallite size of prepared samples was found to be nearly 16 nm. The drastic change in the atomic distribution of A and B spinel sites was confirmed from the Rietveld refinement of XRD. The structure of highly responding N3 films was found almost inverse spinel, as 0.99 fractions of divalent Zn and Ni atoms occupied the octahedral site. The FESEM study confirmed the rough and porous nature of $Ni_{0.3}Zn_{0.7}Fe_2O_4$ thin film. The irregular distribution of random-sized grains on the film surface-enhanced sensing performance as it increases the surface area of the film. The substituted Ni content effects on optimal operating temperature and responses, it reduced the operating temperature of $ZnFe_2O_4$ film. The N3 sample in which 30% of Zn^{2+} ions were replaced with Ni^{2+} ions found better response to SO_2 gas at lowered 130 °C operating temperature. The response and operating temperature of $Ni_{0.3}Zn_{0.7}Fe_2O_4$ thin film were significant over previous SO_2 sensing reports.

Table 5 Operating temperatures of Fe-based SO_2 gas sensing materials

| Material	Sensor form	Operating temperature (°C)	Response	References
$NiFe_2O_4$	Screen-printed thick film	650	ΔV ~ 15 mV 320 ppm	[30]
RGO-loaded $ZnFe_2O_4$	Electrospun nanofibers on chip	350	$\frac{R_a}{R_g}$ 1.8 1 ppm	[31]
Fe_3O_4	Dip-coated film	300	$\frac{\Delta R}{R_0} \times 100$ < 2% 1.2 ppm	[32]
$LaFeO_3$	Pellet	275	$\frac{\Delta R}{R_0} \times 100$ 35% 3 ppm	[33]
$La_{0.8}Ca_{0.2}FeO_{2.95}$			50% 3 ppm	
$LaFeO_3$	Electrospun nanofibers on chip	250	$\frac{\Delta R}{R_0} \times 100$ 90% 1 ppm	[34]
$La_{0.6}Ca_{0.4}FeO_3$	Pellet	160	$\frac{\Delta R}{R_0} \times 100$ 3.6% 5 ppm	[35]
	Thin film	120	$\frac{\Delta R}{R_0} \times 100$ 7.6% 3 ppm	
$Ni_{0.3}Zn_{0.7}Fe_2O_4$	Sprayed thin film	130	$\frac{\Delta R}{R_0} \times 100$ 2.8% 5 ppm	This work
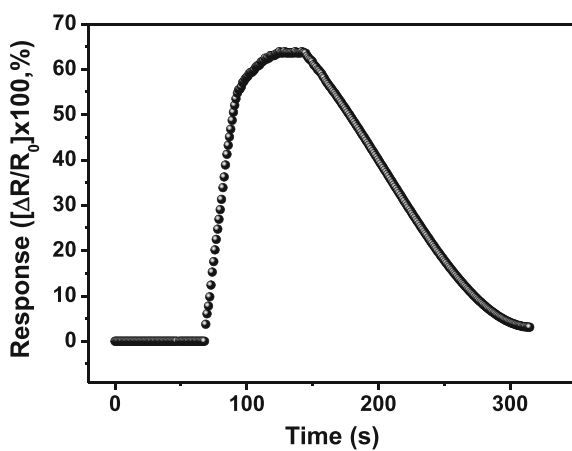
Fig. 6 Response–recovery curve of N3 film at 130 °C
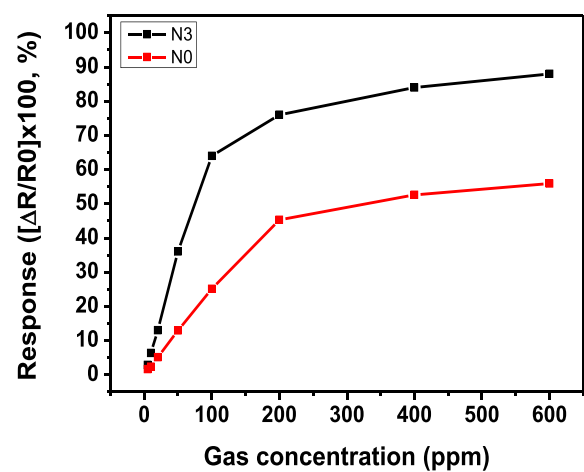

Fig. 7 Variation of the gas response of N0 and N3 films upon exposure of 5 to 600 ppm SO_2 gas at their optimal operating temperature
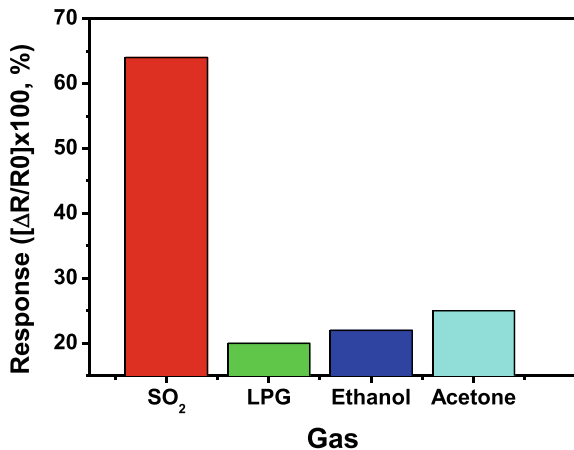
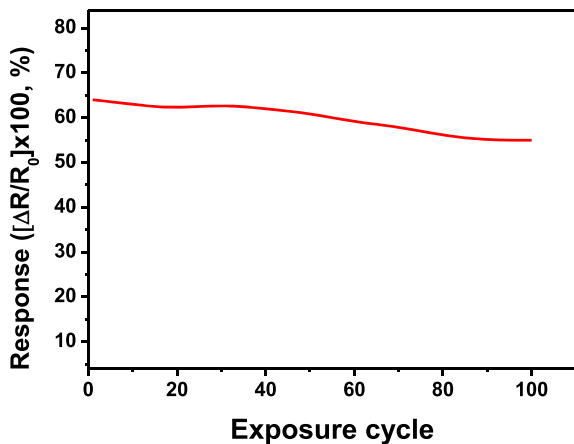**Fig. 8** Response of N3 film toward 100 ppm concentration of various gases at 130 °C operating temperature

Fig. 9 Response of N3 sample for repetitive exposures of 100 ppm SO_2 gas at 130 °C

Acknowledgements

Author contributions

SBM contributed to investigation, methodology, software, and writing and preparation of the original draft. ARP contributed to methodology and software. RSP contributed to software and formal analysis. NAN contributed to visualization and formal analysis. JBT contributed to conceptualization, formal analysis, and writing and preparation of the original draft. KYR contributed to supervision, conceptualization, resource, and writing, reviewing, and editing of the manuscript.

Data availability

The authors confirm that the data supporting the findings of this study are available within the article.

Declarations

Conflict of interest The authors declare that they have no conflict of interest.

References

1. N. Aggarwal, S.B. Narang, Magnetic characterization of Nickel-Zinc spinel ferrites along with their microwave characterization in Ku band. J. Magn. Magn. Mater. **513**, 167052 (2020). https://doi.org/10.1016/j.jmmm.2020.167052
2. A.I. Tovstolytkin, M.M. Kulyk, V.M. Kalita, S.M. Ryabchenko, V.O. Zamorskyi, O.P. Fedorchuk, S.O. Solopan, A.G. Belous, Nickel-zinc spinel nanoferrites: magnetic characterization and prospects of the use in self-controlled magnetic hyperthermia. J. Magn. Magn. Mater. **473**, 422–427 (2019). https://doi.org/10.1016/j.jmmm.2018.10.075
3. T. Tsoncheva, I. Spassova, G. Issa, R. Ivanova, D. Kovacheva, D. Paneva, D. Karashanova, N. Velinov, B. Tsyntsarski, B. Georgieva, M. Dimitrov, N. Petrov, $Ni_{0.5}M_{0.5}Fe_2O_4$ (M = Cu, Zn) ferrites hosted in nanoporous carbon from waste materials as catalysts for hydrogen production. Waste Biomass Valoriz. **12**, 1371–1384 (2021). https://doi.org/10.1007/s12649-020-01094-2
4. S.A. Jadhav, S.B. Somvanshi, M.V. Khedkar, S.R. Patade, K.M. Jadhav, Magneto-structural and photocatalytic behavior of mixed Ni–Zn nano-spinel ferrites: visible light-enabled active photodegradation of rhodamine B. J. Mater. Sci. Mater. Electron. **31**, 11352–11365 (2020). https://doi.org/10.1007/s10854-020-03684-1
5. B. Gayathri Manju, P. Raji, Green synthesis of nickel–copper mixed ferrite nanoparticles: structural, optical, magnetic, electrochemical and antibacterial studies. J. Electron. Mater. **48**, 7710–7720 (2019). https://doi.org/10.1007/s11664-019-07603-x
6. A. Rahman, H. Abdullah, M.S. Zulfakar, M.J. Singh, M.T. Islam, Microwave dielectric properties of $Mn_xZn_{(1-x)}Fe_2O_4$ ceramics and their compatibility with patch antenna. J. Sol-

Gel Sci. Technol. **77**, 470–479 (2016). https://doi.org/10.100
7/s10971-015-3937-4

7. P.T. Phong, P.H. Nam, D.H. Manh, D.K. Tung, I.-J. Lee, N.X. Phuc, Studies of the magnetic properties and specific absorption of $Mn_{0.3}Zn_{0.7}Fe_2O_4$ nanoparticles. J. Electron. Mater. **44**, 287–294 (2015). https://doi.org/10.1007/s11664-014-3463-0

8. M.V. Nikolic, Z.Z. Vasiljevic, M.D. Lukovic, V.P. Pavlovic, J.B. Krstic, J. Vujancevic, N. Tadic, B. Vlahovic, V.B. Pavlovic, Investigation of $ZnFe_2O_4$ spinel ferrite nanocrystalline screen-printed thick films for application in humidity sensing. Int. J. Appl. Ceram. Technol. **16**, 981–993 (2019). https://doi.org/10.1111/ijac.13190

9. V.D. Kapse, S.A. Ghosh, F.C. Raghuwanshi, S.D. Kapse, U.S. Khandekar, Nanocrystalline $Ni_{0.6}Zn_{0.4}Fe_2O_4$: a novel semi-conducting material for ethanol detection. Talanta **78**, 19–25 (2009). https://doi.org/10.1016/j.talanta.2008.10.031

10. A.P. Kazin, M.N. Rumyantseva, V.E. Prusakov, I.P. Suzdalev, A.M. Gaskov, Nanocrystalline ferrites $Ni_xZn_{1-x}Fe_2O_4$: influence of cation distribution on acidic and gas sensing properties. J. Solid State Chem. **184**, 2799–2805 (2011). https://doi.org/10.1016/j.jssc.2011.08.029

11. H.R. Ebrahimi, M. Parish, G.R. Amiri, B. Bahraminejad, S. Fatahian, Synthesis, characterization and gas sensitivity investigation of $Ni_{0.5}Zn_{0.5}Fe_2O_4$ nanoparticles. J. Magn. Magn. Mater. **414**, 55–58 (2016). https://doi.org/10.1016/j.jmmm.2016.04.043

12. S.P. Dalawai, T.J. Shinde, A.B. Gadkari, P.N. Vasambekar, Ni–Zn ferrite thick film gas sensors. J. Mater. Sci. Mater. Electron. **26**, 9016–9025 (2015). https://doi.org/10.1007/s10854-015-3585-z

13. S.B. Madake, M.R. Hattali, K.Y. Rajpure, Porogen induced formation of mesoporous zinc ferrite thin films and their chemiresistive properties. Mater. Sci. Eng. B **263**, 114867 (2021). https://doi.org/10.1016/j.mseb.2020.114867

14. S.S. Kumbhar, M.A. Mahadik, V.S. Mohite, Y.M. Hunge, K.Y. Rajpure, C.H. Bhosale, Effect of Ni content on the structural, morphological and magnetic properties of spray deposited Ni–Zn ferrite thin films. Mater. Res. Bull. **67**, 47–54 (2015). https://doi.org/10.1016/j.materresbull.2015.02.056

15. S.S. Kumbhar, M.A. Mahadik, V.S. Mohite, K.Y. Rajpure, C.H. Bhosale, Synthesis and characterization of spray deposited nickel–zinc ferrite thin films. Energy Procedia **54**, 599–605 (2014). https://doi.org/10.1016/j.egypro.2014.07.301

16. P. Surendran, A. Lakshmanan, S.S. Priya, K. Balakrishnan, P. Rameshkumar, T.A. Hegde, G. Vinitha, G. Ramalingam, A.A. Raj, Investigations on solid-state parameters of third-order nonlinear optical $Ni_{1-x}Zn_xFe_2O_4$ nanoparticles synthesized

by microwave-assisted combustion method. Appl. Phys. A **126**, 257 (2020). https://doi.org/10.1007/s00339-020-3435-6

17. J. Gao, Y. Cui, Z. Yang, The magnetic properties of $Ni_{x-}Zn_{1-x}Fe_2O_4$ films fabricated by alternative sputtering technology. Mater. Sci. Eng. B **110**, 111–114 (2004). https://doi.org/10.1016/j.mseb.2003.10.111

18. D. Guo, Z. Zhang, M. Lin, X. Fan, G. Chai, Y. Xu, D. Xue, Ni–Zn ferrite films with high resonance frequency in the gigahertz range deposited by magnetron sputtering at room temperature. J. Phys. D **42**, 125006 (2009). https://doi.org/10.1088/0022-3727/42/12/125006

19. K. Momma, F. Izumi, VESTA 3 for three-dimensional visualization of crystal, volumetric and morphology data. J. Appl. Crystallogr. **44**, 1272–1276 (2011). https://doi.org/10.1107/S0021889811038970

20. P. Sahoo, Surface topography, in: *Tribology for Engineers* (Elsevier, 2011), pp. 1–32. https://doi.org/10.1533/97808570 91444.1

21. A. Singh, A. Singh, S. Singh, P. Tandon, Fabrication of copper ferrite porous hierarchical nanostructures for an efficient liquefied petroleum gas sensor. Sens. Actuators B **244**, 806–814 (2017). https://doi.org/10.1016/j.snb.2017.01.069

22. X.-Z. Song, Y.-L. Meng, Z. Tan, L. Qiao, T. Huang, X.-F. Wang, Concave $ZnFe_2O_4$ hollow octahedral nanocages derived from Fe-doped MOF-5 for high-performance acetone sensing at low-energy consumption. Inorg. Chem. **56**, 13646–13650 (2017). https://doi.org/10.1021/acs.inorgchem.7b02425

23. Y. Lü, W. Zhan, Y. He, Y. Wang, X. Kong, Q. Kuang, Z. Xie, L. Zheng, MOF-templated synthesis of porous Co_3O_4 concave nanocubes with high specific surface area and their gas sensing properties. ACS Appl. Mater. Interfaces **6**, 4186–4195 (2014). https://doi.org/10.1021/am405858v

24. L. Li, J. Tan, M. Dun, X. Huang, Porous $ZnFe_2O_4$ nanorods with net-worked nanostructure for highly sensor response and fast response acetone gas sensor. Sens. Actuators **248**, 85–91 (2017). https://doi.org/10.1016/j.snb.2017.03.119

25. Y. Zou, H. Wang, R. Yang, X. Lai, J. Wan, G. Lin, D. Liu, Controlled synthesis and enhanced toluene-sensing properties of mesoporous $Ni_xCo_{1-x}Fe_2O_4$ nanostructured microspheres with tunable composite. Sens. Actuators B **280**, 227–234 (2019). https://doi.org/10.1016/j.snb.2018.10.030

26. P. Karthick Kannan, R. Saraswathi, Impedimetric detection of alcohol vapours using nanostructured zinc ferrite. Talanta **129**, 545–551 (2014). https://doi.org/10.1016/j.talanta.2014.06.028

27. Q. Zhou, W. Zeng, W. Chen, L. Xu, R. Kumar, A. Umar, High sensitive and low-concentration sulfur dioxide (SO_2) gas sensor application of heterostructure NiO–ZnO

nanodisks. Sens. Actuators B **298**, 126870 (2019). https://doi.org/10.1016/j.snb.2019.126870

28. L.P. Belo, L.K. Elliott, R.J. Stanger, R. Spörl, K.V. Shah, J. Maier, T.F. Wall, High-temperature conversion of SO_2 to SO_3: homogeneous experiments and catalytic effect of fly ash from air and oxy-fuel firing. Energy Fuels **28**, 7243–7251 (2014). https://doi.org/10.1021/ef5020346

29. M.J. King, W.G. Davenport, M.S. Moats, Catalytic oxidation of SO_2 to SO_3, in: *Sulfuric Acid Manufacture* (Elsevier, 2013), pp. 73–90. https://doi.org/10.1016/B978-0-08-098220-5.00007-1

30. B. Yang, C. Wang, R. Xiao, H. Yu, C. Huang, J. Wang, J. Xu, H. Liu, F. Xia, J. Xiao, High NH_3 selectivity of $NiFe_2O_4$ sensing electrode for potentiometric sensor at elevated temperature. Anal. Chim. Acta **1089**, 165–173 (2019). https://doi.org/10.1016/j.aca.2019.09.006

31. N. Van Hoang, C.M. Hung, N.D. Hoa, N. Van Duy, I. Park, N. Van Hieu, Excellent detection of H_2S gas at ppb concentrations using $ZnFe_2O_4$ nanofibers loaded with reduced graphene oxide. Sens. Actuators B **282**, 876–884 (2019). https://doi.org/10.1016/j.snb.2018.11.157

32. Y.-J. Hsiao, Y. Nagarjuna, C.-A. Tsai, S.-C. Wang, High selectivity Fe_3O_4 nanoparticle to volatile organic compound (VOC) for MEMS gas sensors. Mater. Res. Express **7**, 065013 (2020). https://doi.org/10.1088/2053-1591/ab9bc7

33. S. Palimar, S.D. Kaushik, V. Siruguri, D. Swain, A.E. Viegas, C. Narayana, N.G. Sundaram, Investigation of Ca substitution on the gas sensing potential of $LaFeO_3$ nanoparticles towards low concentration SO_2 gas. Dalton Trans. **45**, 13547–13555 (2016). https://doi.org/10.1039/C6DT01819J

34. A. Queraltó, D. Graf, R. Frohnhoven, T. Fischer, H. Vanrompay, S. Bals, A. Bartasyte, S. Mathur, $LaFeO_3$ nanofibers for high detection of sulfur-containing gases. ACS Sustain. Chem. Eng. **7**, 6023–6032 (2019). https://doi.org/10.1021/acssuschemeng.8b06132

35. C. Aranthady, T. Jangid, K. Gupta, A.K. Mishra, S.D. Kaushik, V. Siruguri, G.M. Rao, G.V. Shanbhag, N.G. Sundaram, Selective SO_2 detection at low concentration by Ca substituted $LaFeO_3$ chemiresistive gas sensor: a comparative study of $LaFeO_3$ pellet vs thin film. Sens. Actuators B **329**, 129211 (2021). https://doi.org/10.1016/j.snb.2020.129211

Publisher's Note Springer Nature remains neutral with regard to jurisdictional claims in published maps and institutional affiliations.